

RESEARCH

Open Access



Archaeological cognition of the Eastern mausoleum of Qin state using integrated space-ground observation tools

Yansong Luo^{1,2,3}, Fulong Chen^{1,2,4*}, Sheng Gao^{1,2,3}, Meng Zhu^{1,2,4}, Wei Zhou^{1,2,4} and Abdelaziz Elfadaly⁵

Abstract

The Eastern Mausoleum of Qin State is a significant component of the Qin Dynasty's royal tombs, reflecting the social development level during the Warring States period (475 BC ~ 221 BC) in China. At the onset of our investigation, we mapped the site's boundaries utilizing Corona satellite imagery and employed the Normalized Difference Vegetation Index (NDVI) and Normalized Difference Moisture Index (NDMI) to identify archaeological features. Additionally, this study is the first to propose the use of thermal infrared band data from the SDGSAT-1 satellite to explore thermal archaeological traces, demonstrating their viability for archaeological site analysis. Subsequently, electromagnetic (EM) prospecting was utilized to validate the presence of an ancient burial chamber passage. Landscape monitoring and analysis of the No.1 Mausoleum were performed using Corona and Google Earth images, revealing the accuracy of the Geomancy Theory of Chinese mausoleums through dynamic remote sensing of surface changes. Furthermore, our employment of space-to-ground observational modalities and resultant Digital Elevation Models (DEM) have been used to provide new insights into the application of Remote Sensing (RS) and Geomancy in archaeology, thereby emphasizing the pivotal role of site selection in heritage preservation. This research underscores the promise of synergistic space-ground observations in both exploiting the archaeological riches of cultural heritage sites and ensuring the enduring conservation of these irreplaceable patrimonial assets.

Keywords Remote sensing, Archaeology, Eastern mausoleum of Qin State, Site selection, Electromagnetic prospecting

Introduction

Recognizing the importance of heritage, the United Nations' Sustainable Development Goals (SDGs) include Target 11.4, which aims to "Strengthen efforts to protect

and safeguard the world's cultural and natural heritage," thereby officially establishing heritage as an irreplaceable SDG indicator. As a non-renewable resource, cultural heritage serves as a testament to the evolution of human civilization and ensures the continuation of cultural traditions. Its unique status has led to the sustainable protection and utilization of cultural heritage becoming a focus in archaeological research [1–4].

China has gone through several dynasties and has a vast amount of excavated both and unexplored cultural heritage sites. The Eastern Mausoleum of Qin State (hereafter referred to as the Mausoleum), as the first large-scale feudal emperor's tomb in Chinese history, involves complex factors such as geography, geomancy, politics, and culture in its site selection [5–8]. It holds

*Correspondence:

Fulong Chen
chenfl@aircas.ac.cn

¹ Key Laboratory of Digital Earth Science, Aerospace Information Research Institute, Chinese Academy of Sciences, Beijing 100094, China

² International Research Center of Big Data for Sustainable Development Goals, Beijing 100094, China

³ University of Chinese Academy of Sciences, Beijing 100049, China

⁴ International Centre On Space Technologies for Natural and Cultural Heritage Under the Auspices of UNESCO, Beijing 100094, China

⁵ National Authority for Remote Sensing & Space Sciences, Cairo 1564, Egypt



© The Author(s) 2024. **Open Access** This article is licensed under a Creative Commons Attribution 4.0 International License, which permits use, sharing, adaptation, distribution and reproduction in any medium or format, as long as you give appropriate credit to the original author(s) and the source, provide a link to the Creative Commons licence, and indicate if changes were made. The images or other third party material in this article are included in the article's Creative Commons licence, unless indicated otherwise in a credit line to the material. If material is not included in the article's Creative Commons licence and your intended use is not permitted by statutory regulation or exceeds the permitted use, you will need to obtain permission directly from the copyright holder. To view a copy of this licence, visit <http://creativecommons.org/licenses/by/4.0/>. The Creative Commons Public Domain Dedication waiver (<http://creativecommons.org/publicdomain/zero/1.0/>) applies to the data made available in this article, unless otherwise stated in a credit line to the data.

significant archaeological importance, and studying it can provide valuable insights for research on other sites. Although extensive research has been conducted since its rediscovery in 1986, comprehensive exploration of the tomb's interior has been limited due to excavation and heritage protection constraints [9–11]. Therefore, there is an urgent need to utilize archaeology for multi-dimensional and multi-faceted exploration.

Over several decades, archaeology has evolved, with current methodologies encompassing both remote sensing and fieldwork. In Ref. [12–16]. Remote sensing techniques, such as aerial photography, ground-penetrating radar, and soil resistance surveys, offer multiple advantages but also encounter limitations, including high costs and spatial constraints. Advanced technologies such as Airborne Light Detection and Ranging (LiDAR) and multispectral remote sensing remain somewhat underutilized [17, 18].

RS endorsed by UNESCO, has been employed to bridge the gaps in archaeological research, which serves as an efficient monitoring tool, utilizing indicators like land cover and land change analysis [19–22]. Numerous studies have been conducted utilizing multi-mode, multi-spectral image acquisition for information extraction and site condition monitoring [23–27]. Additionally, archaeological signatures, such as vegetation, moist soils, and thermal archaeological traces, are the primary methods of site analysis. Archaeological features are often subtle or even imperceptible; however, RS-based feature extraction and enhancement techniques assist in identifying these anomalies. Among these, thermal infrared remote sensing, which captures Earth's surface radiative energy, plays a pivotal role in regional temperature mapping and archaeological studies [28]. The SDGSAT-1 satellite, launched in 2021, provides high-resolution wide-field Thermal Infrared Spectrometer (TIS) [29], but fewer studies are currently putting them to use, which this study leverage for investigating thermal anomalies in the Mausoleum.

However, relying solely on space-based site exploration is overly uniform. Geophysical prospection is a standard method for detecting buried archaeological features and structures, commonly used to validate the applicability of vegetation, soil, and thermal archaeology traces [30], such as using the GEM-2 electromagnetic exploration instrument, complement RS techniques by detecting buried archaeological features and structures. These methods enable non-contact, non-destructive investigations, making them particularly suitable for ancient heritage sites [31, 32]. Changes in heritage conditions pose threats to the authenticity and integrity of heritage properties [33, 34]; This study emphasizes the need for non-destructive exploration and cultural heritage preservation,

combining remote sensing and field archaeology to enhance research outcomes' scientificity and reliability.

Currently, the integration of remote sensing and electromagnetic prospecting for identifying archaeological markers at burial sites is infrequent, and studies of surface temperature inversion predominantly utilize thermal infrared data from the Landsat and MODIS series [35]. In addition to employing standard indices like NDVI and NDMI to detect anomalies indicative of archaeological markers, this research utilized Corona satellite imagery to delineate the site boundary and innovatively applied thermal infrared band data from the SDGSAT-1 satellite to detect thermal anomalies at the Eastern Mausoleum of the Qin State, a method still underutilized in archaeological research. Furthermore, the combination of ground-based electromagnetic geophysical prospecting with multi-mode satellite observations provides a comprehensive understanding of the site, enhancing the accuracy of archaeological investigations. This dual approach confirms the viability of remote sensing technologies in archaeology and emphasizes the necessity of dynamic monitoring for sustainable heritage conservation. Additionally, the utilization of DEM derived from remote sensing data offers a novel perspective on the site selection process, particularly in the context of Chinese Geomancy Theory. This approach demonstrates the potential of combining remote sensing with geophysical techniques in heritage preservation and archaeological research, laying a foundation for future studies in similar contexts.

Materials and methods

Study site and data

Xi'an, formerly known as Xianyang in the pre-Qin and Qin period before 207 BC, and as Chang'an during the Han period from 202 BC to 220 AD and the Tang period from 618 to 907 AD, boasts a history of over 3,100 years of city building and more than 1,100 years as the national capital of China. Thirteen dynasties, including the pre-Qin State and Qin Dynasty, established their capitals here. After nine capital relocations, Xianyang's selection as the capital secured the hegemony of the Qin State. Following the Bimo Cemetery in Xianyang, the Mausoleum served as the royal tomb before the Mausoleum of the First Qin Emperor during the Warring States period. As the first large-scale feudal imperial tomb in Chinese history, the Mausoleum profoundly influenced tomb architecture and imperial funerals for generations. Its rigorous architectural planning and massive engineering projects set standards for subsequent feudal imperial tombs.

The Mausoleum, also known as the Zhiyang Mausoleum, is located at the western foothills of Lishan Mountain in Lintong, Xi'an City, China. It stretches from

Hongqing Gully in the south to Wangpo Gully (Wujia Gully) in the north, covering an area of approximately 24 square kilometers (Fig. 1). Archaeological prospecting at this site is crucial for uncovering the civilization of the pre-Qin period, which dates back two thousand years. Due to the site's vast dimensions, the No.1 Mausoleum was selected for focused investigation in this study. The geographic coordinate system used is GCS_WGS_1984, and the projection coordinate system is WGS_1984_UTM_Zone_49N.

To enhance the identification of vegetation and soil anomalies related to archaeological traces, a series of multi-temporal Sentinel-2 images (30 m) from Google Earth Engine (GEE) was utilized. These images provide a spatial resolution of up to 10 m in the Blue, Green, Red, and NIR bands, while the Vegetation Red Edge and SWIR bands have a 20-m resolution. The image collection spans

from January 2016 to December 2018 to avoid disturbances related to field excavations conducted since 2019. Additionally, six scenes of thermal infrared spectrometer images from SDGSAT-1, featuring a spatial resolution of 30 m, were acquired during the summer and winter seasons of 2022, and the spring of 2023. This approach minimizes the influence of chance errors and enables a comparison of inversion results across different seasons and times. Synchronously, Level 1B Calibrated Radiances-1km (MOD02) and Terra Land Surface Temperature/Emissivity 5-Min L2 Swath 1km (MOD11_L2) data were collected for NDVI calculations and to validate inversion results. Additionally, two sets of RS images were acquired to detect landscape changes. The first set includes Corona imagery captured in May 1970, with an approximate spatial resolution of 2 m, and the second set includes high-resolution GEE imagery. Electromagnetic

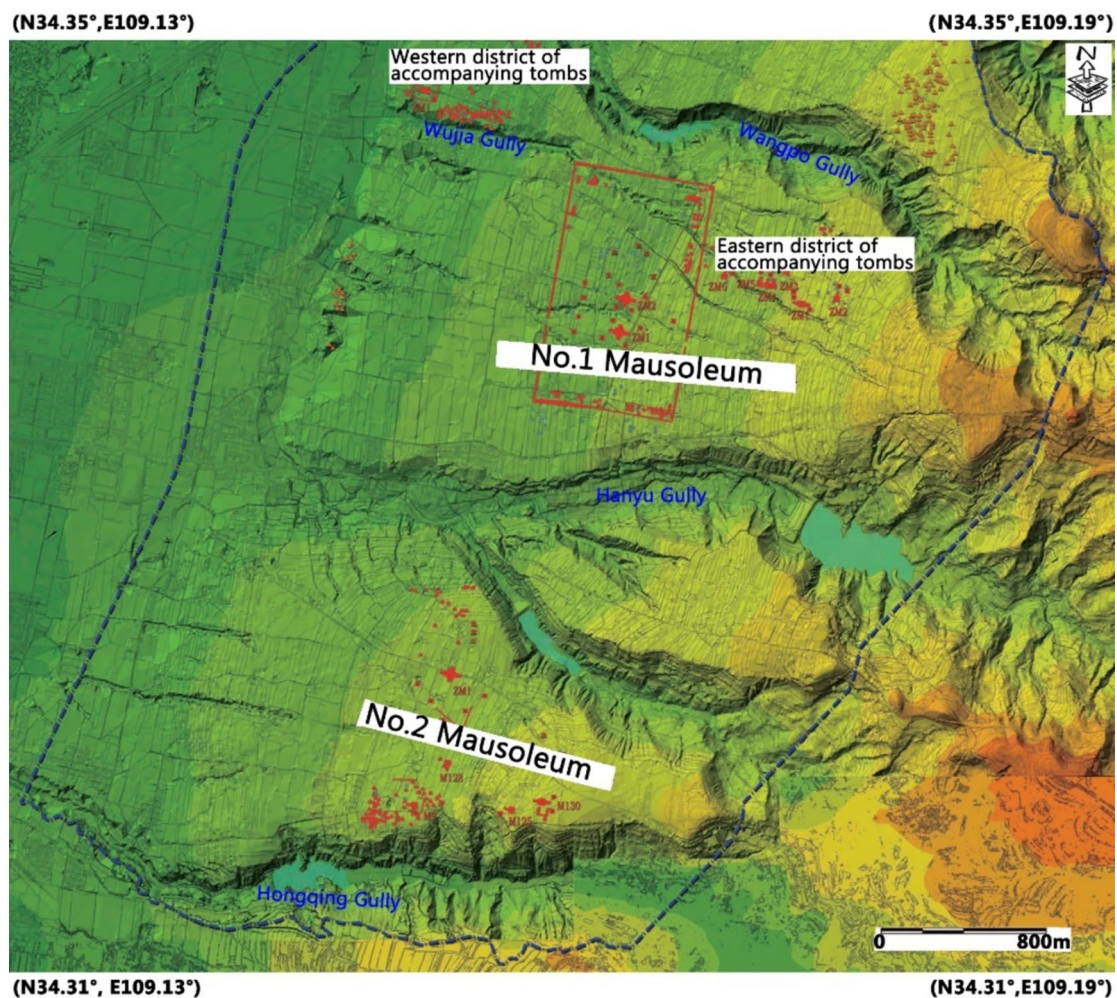


Fig. 1 The location of the Eastern Mausoleum of Qin State, and the No.1 Mausoleum was selected for the investigation; the background imagery is from [36]

prospecting with the GEM-2 instrument was conducted to investigate the surface of a section of Tomb ZM2 in the No.1 Mausoleum (Fig. 1), to cross-validate the occurrence of archaeological signatures in RS images of ancient traces. This physical exploration covered a spatial range of 70 m by 4.5 m on June 14, 2023. The GEM-2 multi-frequency electromagnetism covers a frequency range from 25Hz to 93kHz, and can operate simultaneously at multiple frequencies. In this study, five frequencies were selected for data collection: 3025Hz, 6325Hz, 13175Hz, 27525Hz, and 57525Hz, to obtain electrical conductivity values from different depths, ranging from the surface to several meters deep. Topographic and landscape analysis was conducted using 1 arc-second Shuttle Radar Topography Mission (SRTM) DEM data (30 m) to verify the optimized site selection of royal tombs.

Method and data processing

In archaeological research, relying on a single observational method often presents limitations. Space-based observation tools, such as satellite remote sensing, provide large-scale data that enable the identification of surface anomalies, such as vegetation and soil moisture changes, and can even detect subtle thermal anomalies through infrared imaging. However, the resolution of these tools may be constrained by sensor capabilities, particularly when investigating subsurface structures. Remote sensing data often lack the precision and depth needed to directly reveal deeply buried archaeological remains.

On the other hand, ground-based observation tools, such as electromagnetic prospecting, offer more precise localized information, especially for detecting subsurface structures with higher resolution. However, their coverage is limited, making it difficult to provide a comprehensive overview of large sites. Consequently, relying solely on ground-based tools may overlook important macro-level archaeological clues, particularly for large-scale sites, where localized high-resolution detection fails to capture the site's overall characteristics.

To address these challenges, this study employs an integrated approach that combines space-based and ground-based observation tools. By first using space-based observation tools for a wide-area preliminary survey, we can quickly identify potential archaeological target areas. These areas are then further explored with ground-based electromagnetic prospecting tools for more precise and detailed investigation. This integrated approach not only compensates for the limitations of single methods in terms of coverage and resolution, but also enables multi-scale observation, from macro to micro levels. The combination of large-scale spatial coverage with localized high-resolution detection allows for a more

comprehensive and accurate understanding of both surface and subsurface features of the site.

To deepen the understanding of the archaeological exploitation of the Mausoleum (Xi'an, China), an integrated approach involving space-ground observations, feature extraction, and cognitive knowledge was employed, as shown in Fig. 2.

Archaeological marks

Satellite remote sensing imagery can effectively detect archaeological features on the surface and in shallow subsurface layers. Compared with the surrounding areas, exposed and shadow-buried relics alter the physical, chemical properties, and other relevant parameters of the observed surface, resulting in the albedo and backscatter signature anomalies on the remotely sensed images, characterized by regular geometric shapes and image textures, which include soil dampness, vegetation, and shadow archaeological marks [37–39]. As a result, ancient surface landscapes have been subjected to centuries of disturbance, leading to dynamic changes. To effectively extract archaeological targets, it is necessary to employ a variety of remote sensing image processing and enhancement methods to capture subtle information. Common remote sensing methods for archaeological detection include histogram transformation [40], and data fusion algorithms [41–44], as in the case of PCA (Principal Component Analysis), HIS data fusion techniques and Gaussian high-pass, which were utilized to survey the site by enhancing weak archaeological information. For this study, the 1970 Corona imagery was employed for extraction in the area of the No.1 Mausoleum site.

NDVI is used to monitor the distribution, growth, and health of vegetation, as well as changes in surface cover; NDMI monitors soil moisture, surface moisture status, and the relationship between vegetation and moisture [45–48]. In this study, ensemble-averaged indices of NDVI and NDMI were employed to characterize the vegetation and soil marks associated with royal tombs. While the depth of coffin chambers in royal tombs can exceed 20 m, making related archaeological traces negligible, other archaeological features, such as burial chamber passage, are buried at shallower depths and may be detected due to alterations in the physical properties of rammed earth. To reduce cloud impact, geometric and radiometric corrections were applied to a time series of Sentinel-2 images using Google Earth Engine (GEE). A total of 93 multispectral image scenes were analyzed to calculate NDVI and NDMI, followed by temporal averaging.

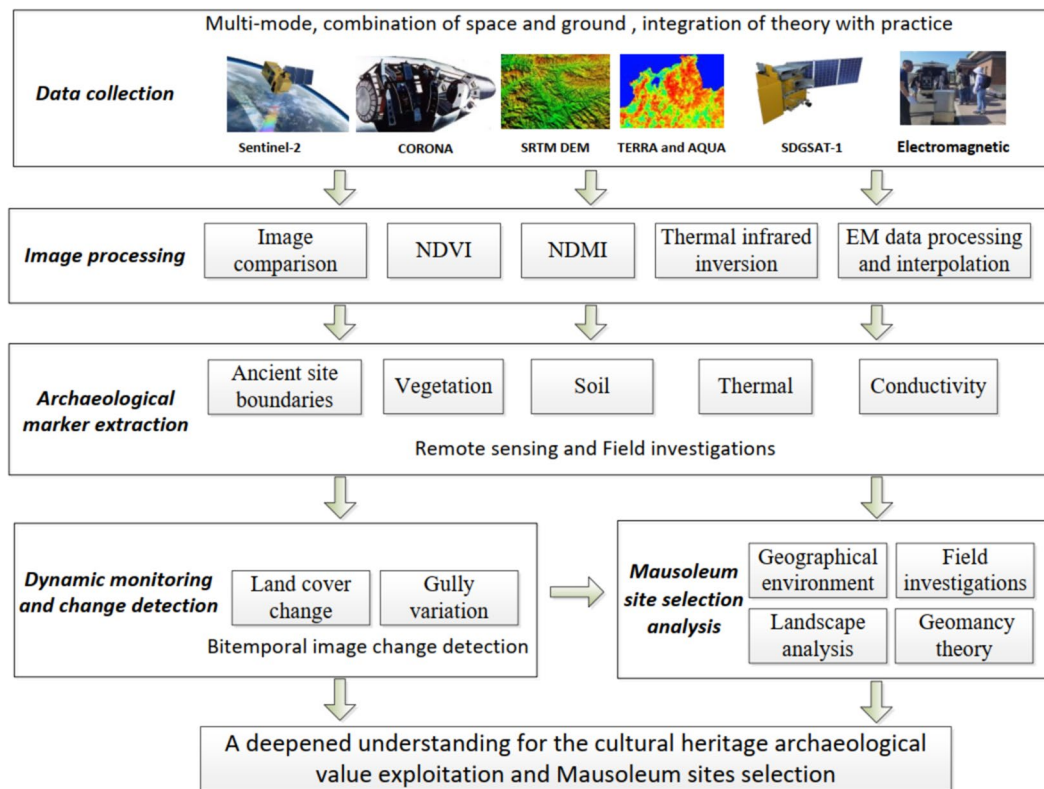


Fig. 2 Working flowchart for the archaeological prospecting for the Eastern Mausoleum of Qin State

$$NDVI = (NIR - R)/(NIR + R) \quad (1)$$

$$NDMI = (NIR - SWIR)/(NIR + SWIR) \quad (2)$$

where NIR , R , and $SWIR$ are the near-infrared, red, and short-wave infrared bands of multi-spectral images, respectively.

Thermal anomalies, which are inferred from satellite thermal infrared data, represent another effective indicator of archaeological features. Thermal infrared images from SDGSAT-1 were analyzed using the single-window algorithm for this study [49–52]:

$$T_s = \{a(1 - C - D) + [b(1 - C - D) + C + D]T_b - DT_a\}/C \quad (3)$$

$$C = \tau\varepsilon \quad (4)$$

$$D = (1 - \varepsilon)[1 + (1 - \varepsilon)\tau] \quad (5)$$

where T_s is the inverted surface temperature; T_b is the brightness temperature obtained by the sensor; T_a is the mean atmospheric action temperature, equivalent to the value of the time-air temperature obtained from historical weather data; a and b are the regression coefficients; C and D are the intermediate variables, τ is the atmospheric

transmittance rate, and ε is the surface emissivity. Referring to the results [53], the values of a and b are taken as -67.355351 and 0.458606, respectively. The formula for calculating T_b , as well as the wavelength, gain, and bias (calibration parameters) of the corresponding bands, is recorded in the SDGSAT-1 satellite user manual[54]. The downloaded thermal infrared images were pre-processed, radiometrically calibrated, and the Digital Number (DN) values were converted to radiance. Planck's equation was subsequently applied to convert the radiance into the satellite's effective on-orbit brightness temperature.

Note that surface emissivity, which characterizes the magnitude of emissivity, is one of the most critical parameters in surface temperature inversion, with values ranging between 0 and 1. In this study, land use types in the study area were categorized into four categories: water bodies, natural surfaces, towns, and bare soil, using supervised classification. 'Natural surface' refers to areas covered with vegetation, such as farmland, woodland, and grassland; while 'towns' refer to urban and rural areas with roads, houses, and buildings. Surface emissivity values for vegetation, buildings, and bare soil were assigned values of 0.986, 0.970, and 0.972, respectively, while the surface emissivity for water was set at 0.995 [55–58]. Additionally, atmospheric transmittance,

the ratio of the energy of surface radiation that passes through the atmosphere to the remote sensor, was calculated. Considering the atmospheric water vapor content was not obtainable from the TIS image, the channel ratio method was applied to invert this indicator based on the MOD02 band 2 and band 19 data [59, 60]. This calculation took into account the absorption and reflection of atmospheric water vapor content [61].

The surface temperature was inverted using the calculated parameters mentioned earlier to identify any thermal anomalies in the No.1 Mausoleum. Among various geophysical exploration techniques, the electromagnetic method offers significant advantages for shallow geophysical exploration. In this study, electromagnetic prospecting was performed using the GEM-2 instrument to collect on-site physical probe data. Subsequently, the Invertor software was employed to derive values for apparent electrical conductivity and apparent magnetization rate (milliSiemens per meter, mS/m). The use of broadband, multi-frequency electromagnetic sensors provide notable benefits. Utilizing multiple frequencies is advantageous due to the skin-depth effect, which is inversely proportional to frequency: low-frequency signals penetrate deeper into the conductive earth, revealing deeper structures, while high-frequency signals only penetrate shallow depths, exposing near-surface structures. Therefore, scanning through the frequency spectrum is essential for depth detection. Figure 3 presents

a nomogram that determines the skin depth for a given frequency.

Change detection

The attainability of heritage sites faces challenges due to the induced disturbance from the alteration of the cultural landscape as well as the degradation of heritage ontology, which threaten the authenticity and integrity of heritage’s historical, artistic, or scientific values. Owing to the macro, fast, objective, and quantitative observation capability, RS has played an irreplaceable tool in cultural heritage monitoring.

This study compared bitemporal Corona and GEE images for cultural landscape change detection. Firstly, the true-color GEE imagery was transferred into grey-scale imagery. Then, Corona imagery was co-registered with the GEE imagery using a second-order polynomial function based on the manually extracted tie-points on road intersections, historical building corners, and farmland corners. After that, the pixel-based change detection approach was employed for the change patch detection (note that, the salt-to-pepper noise and false noise due to registration have been removed using the threshold of changed patches). We further analyze the surface change through the development trajectory of gullies. RS extracted the alteration of the gully’s geometry in terms of length, which in turn reveals the intensity of surface change in the observation span.

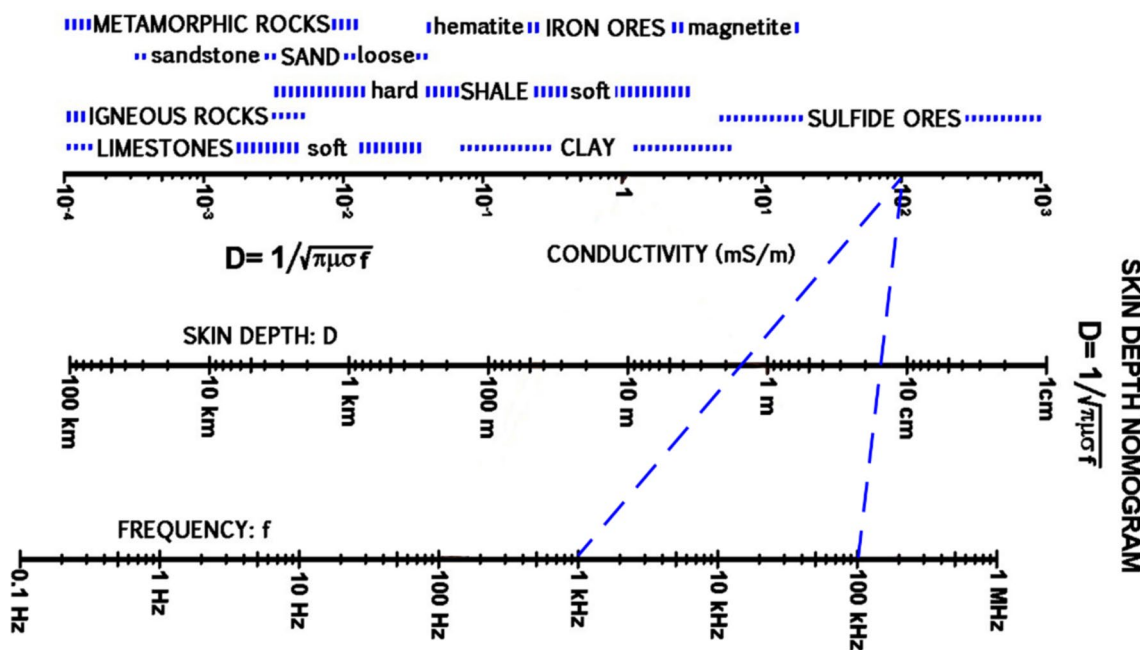


Fig. 3 Relationship among source frequency, ground conductivity, and penetration depth. For example, if the source frequency sweeps from 1 to 100 kHz, the depth of exploration (skin depth) ranges from about 0.18 m to 1.8 m [62]

Landscape analysis for the site selection

Chinese Geomancy Theory, which was crucial in the site selection of royal tombs in ancient China, can now be thoroughly illustrated through celestial eye landscape analysis. Firstly, environmental elements such as rivers, lakes, wetlands, hills, mountains, and artificial features like the capital city, main roads, and residential areas are mapped using uniform geographical coordinates. Secondly, the orientation relationships and intervisibility between these environmental elements and artificial features are quantitatively analyzed by overlaying ortho-images on terrain layers. Thirdly, the site's resilience to natural disasters, such as flooding, is intuitively demonstrated using terrain data (i.e., relatively higher terraces) coupled with hydrological analysis for flooding mitigation. Thus, the evidence supporting the optimized site selection for tombs, adhering to Chinese Geomancy Theory, can be vividly demonstrated with indicators for viewing effect and disaster avoidance.

Results

Remote sensing archaeology

Initially, we used Corona images to extract and identify the site, applying both the NDVI and NDMI to highlight archaeological traces. Furthermore, we utilized thermal infrared band data from the SDGSAT-1 satellite to explore and reveal enhancements in thermal archaeological signs. Subsequently, electromagnetic prospecting was employed to confirm the presence of an ancient tomb passage.

Site extraction and identification

In the semi-humid continental monsoon climate of the warm temperate zone where the Mausoleum is located, the surface conditions vary significantly. Due to the complex interactions between crop marks, surface cover, and phenological periods, these marks may not be effective for archaeological detection. Consequently, the following image enhancement methods were sequentially utilized. Figure 4 illustrates the results of applying high-pass Gaussian filtering, Sobel edge detection, texture analysis, and post-processing techniques like image thresholding to Corona imagery[63]. The derived result clearly delineates the boundary between the Mausoleum and the surrounding areas, as indicated by the red line in Fig. 4b. These results underscore the feasibility of using historical imagery to detect ancient sites.

Vegetation and soil marks

Figure 5 illustrates the vegetation and soil archaeological marks identified by the NDVI and NDMI indices, calculated from multispectral Sentinel-2 images acquired from January 2016 to December 2018. Artificial features such as roads and buildings, as well as water bodies, show lower NDVI values compared to crop areas. Gully regions exhibit the highest values, attributed to the presence of trees. While not immediately apparent, the subset in Fig. 5a shows a suppressed NDVI value near the royal tomb of No.1 Mausoleum. The NDMI mark over the royal tomb area is subtle, as shown in Fig. 5b, likely due to the deeply buried cultural relics and the minimal archaeological signature detectable from the surface.

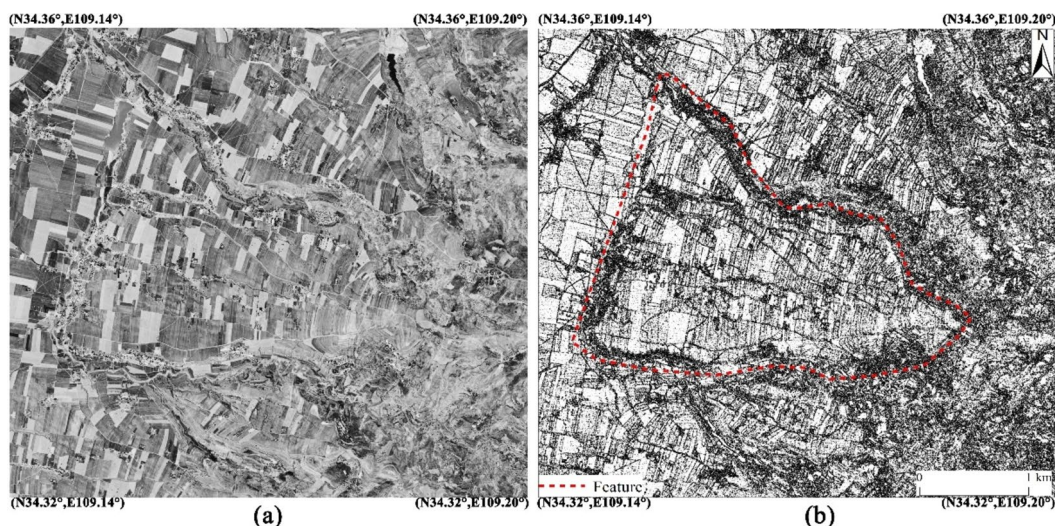


Fig. 4 Corona-based automatic extraction of archaeological sites. **a** original Corona satellite image from 1970; **b** after image processing and enhancement

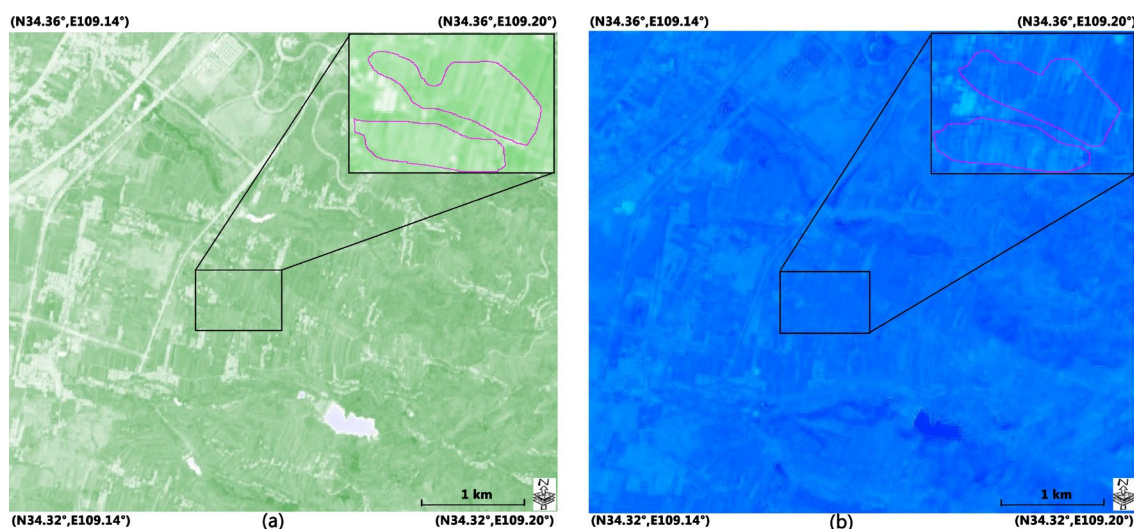


Fig. 5 Archaeological marks on the No.1 mausoleum of the Eastern Mausoleum of Qin State. **a** The vegetation mark with greener color indicates greater NDVI values, and the subset imagery in the top-right shows the original resolution of average NDVI value; **b** soil mark with bluer color indicates greater NDMI values, the subset imagery in the top-right shows the original resolution of average NDMI value covering the area of royal tombs

Thermal marks

In addition to using NDVI and NDMI for identifying vegetation and soil archaeological imprints, thermal signatures were also examined. Following the single-window algorithmic principle, surface temperatures were computed at six distinct acquisition times, each involving three bands of thermal infrared data, resulting in a total of 18 thermal images processed using ENVI and ArcMap software suites. Notably, the temperatures from Band1 of the Thermal Infrared Sensor (TIS) showed significant discrepancies compared to those from the Moderate-resolution Imaging Spectroradiometer Land Surface Temperature product (MODIS MOD11_L2). Figure 6 illustrates the mean values of the surface temperatures for Band2 and Band3 inversions in TIS. High surface temperature values are primarily concentrated in areas of rock formations, soil, and artificial structures with strong thermal radiation characteristics, as observed from the overlaid inverted surface temperatures and RS images. During summer, urban areas exhibit higher surface temperatures, while vegetated areas show lower temperatures.

Surface temperatures at the No.1 Mausoleum predominantly show medium–low values with some scattered medium–high temperatures (Fig. 6a, b). A similar pattern is observed during the winter, despite the absence of vegetation cover (Fig. 6c–f). Notably, most areas of the No.1 Mausoleum in Fig. 6c display lower values, highlighting thermal archaeological features. Typically, the amplitude trend of temperature measurements is reversed, with higher values in urban areas and lower

values in vegetated areas during the summer, and the opposite during the winter (Fig. 6b, d). It is important to note that temperature inversion may be influenced by the accuracy of MOD02 data and cloud cover interference, leading to consistently lower or higher temperature readings (Fig. 6f). Overall, detecting temperature differences due to archaeological features is feasible, as illustrated in Fig. 6c, although the boundaries of hotspots may not be distinctly marked. Moreover, selecting the appropriate observation window for thermal images is crucial in detecting thermal archaeological marks, especially to mitigate potential aliasing caused by uneven daytime irradiation and nighttime vegetation disturbances.

Since actual surface temperature measurements were not available for the study area, MOD11_L2 data were employed to validate the accuracy of the temperature inversion. The spatial resolution of TIS temperature images (30 m) was resampled to match the 1000 m resolution of MODLT data. A statistical average was used for the comparison, as listed in Table 1. In line with previous studies[64], the surface temperatures inverted using the single window algorithm generally trend lower than those from MODLT. An exception was observed on 9 July 2022, where a notable discrepancy was noted, attributed to an anomalous MODLT value of 40.19 °C in the early morning. Nonetheless, the residual measurements between these two data sources remain consistent, with differences ranging from -5.28 °C to -3.28 °C.

Since NDVI, NDMI, and thermal archaeological markers are present in the No. 1 Mausoleum, albeit in weak

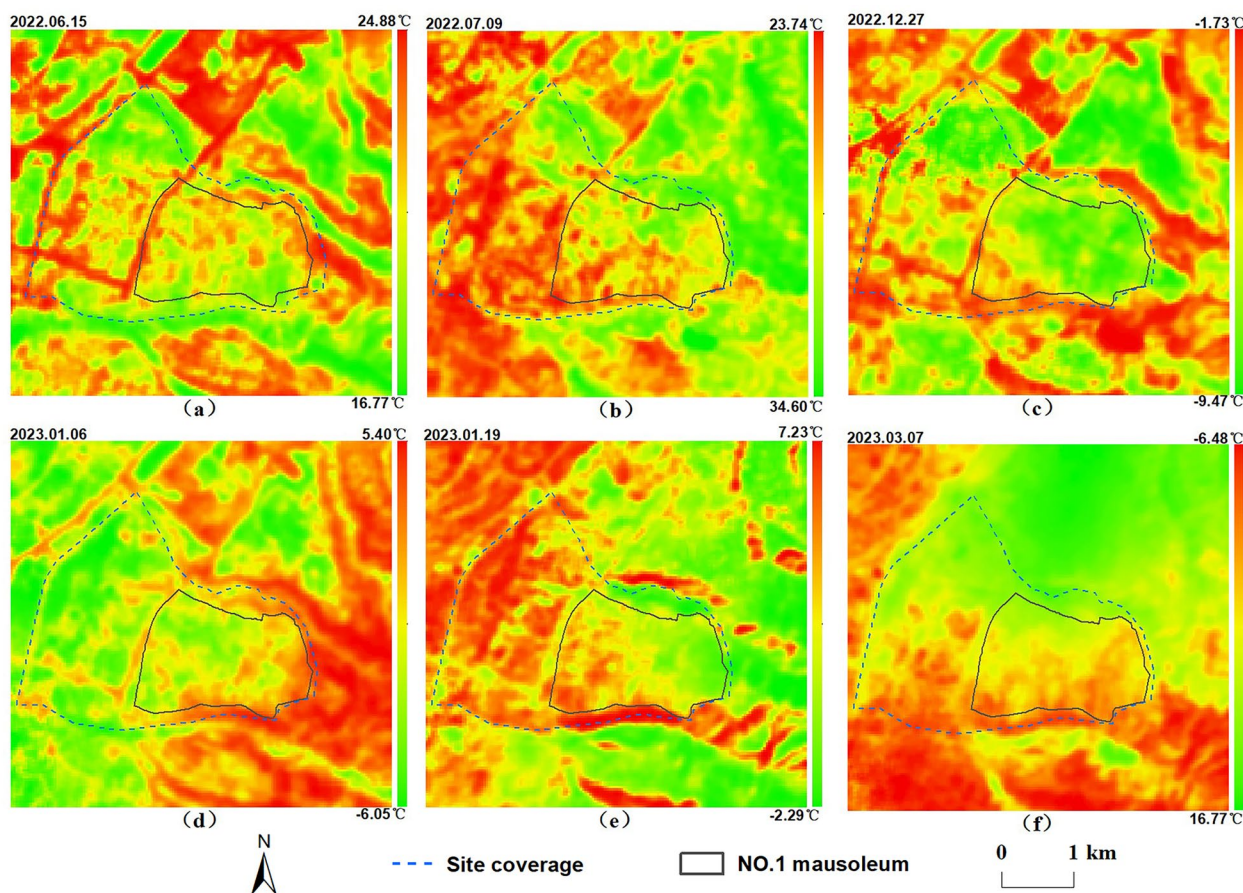


Fig. 6 Thermal archaeological marks on the No.1 mausoleum of the Eastern Mausoleum of Qin State: **a)** and **b)** measurements in summer seasons; **c–f)** measurements in winter seasons. The thermal archaeological mark is more evident in **c)**. Figure 6 has the same scope as Fig. 5

intensity, a fieldwork expedition around it was undertaken to confirm their suitability for the ancient tomb.

Field investigations

Figure 7 details the soil structure in the electromagnetic prospecting area’s profile, highlighting the layers and soil types with a color line distinguishing between raw and compacted soils. Close-up images (Fig. 7b, c) depict the texture and structure of these soils, while the image maps (Fig. 7d) show the study area and specific observation points. On-site observations reveal distinct soil stratification. The upper soil layer, lighter in color and looser in texture, displays signs of prior collapse, suggesting it is virgin soil. In contrast, the lower soil layer is darker and more compact, with no collapse signs, indicating human intervention and classifying it as rammed earth.

Based on these observations, an electromagnetic prospecting was conducted using the GEM-2 instrument to evaluate the applicability of space remote sensing

Table 1 Comparison of surface temperature measurements between SDGSAT-1 TIS and MODLT data

Time	Temperature/°C		
	SDGSAT-1	MODLT	Difference
2022.06.15 pm	21.48	24.77	– 3.29
2022.07.09 am	28.57	40.19	– 11.62
2023.01.06 am	– 0.01	4.22	– 4.23
2023.01.19 pm	2.67	7.95	– 5.28

techniques in archaeology. The investigation, conducted over an area measuring 70 m by 4.5 m, demonstrated that the detection depth decreases with increasing frequency when using the GEM-2 object finder. Figure 8a shows the distribution of conductivity contours at frequencies of 3025 Hz, 6325 Hz, 13,175 Hz, 27,525 Hz, and 57,525 Hz, generated using the Kriging interpolation method and Surfer software.

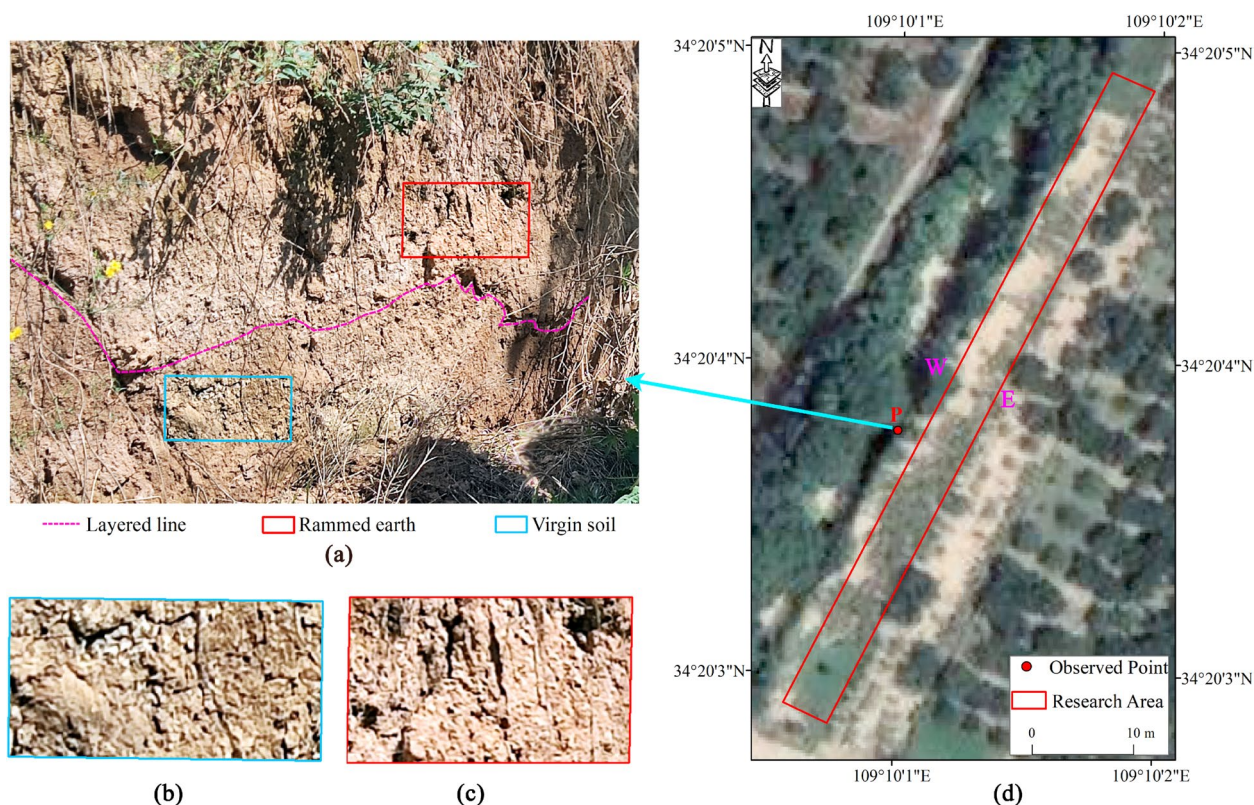


Fig. 7 Represents the soil conditions in the electromagnetic prospecting area. **a** represents a cross-sectional view of the soil at observation point P, which corresponds to the left view of the electromagnetic prospecting area; **b** illustrates a more typical virgin soil; **c** depicts a more typical rammed earth; **d** presents an aerial view of the electromagnetic prospecting area, define the side where point P is located as the west side(W) of the research area and the opposite side as the east side(E)

Apparent conductivity is a commonly used parameter for interpreting electromagnetic data, offering a more intuitive reflection of electrical variations in the subsurface compared to the original data and providing initial model parameters for subsequent quantitative inversion[65]. These conductivity contours are organized based on their depth from the surface, from top to bottom (Fig. 8).

When observed from point P, the conductivity distribution in the first and second layers follows a more regular pattern, with low values in the middle and high values at both ends. Most of the low values are concentrated at one end of the observation area. The third layer through the fifth layer does not exhibit a clear pattern, but the majority of low values are located near point P. Theoretically, point P is situated in the middle of the layer, where the conductivity contours are found. In theory, the face where point P is located represents a cliff face, which is more affected by sunshine and rainfall. Given that the data collection occurred during summer, the conductivity should be lower on this side (west side). On the opposite side (east side), which is less affected by higher water

content, the conductivity is higher. Figure 8b presents the processed results of the physically detected points after manual adjustments, includes removal of invalid points and image processing, such as image enhancement and stretching. It reveals a more pronounced pattern of electrical conductivity distribution, consistent with theoretical expectations. The electrical conductivity of each layer is lower on west side, and higher on the east side. Similar to Fig. 8a, the lower values are primarily concentrated near point P, confirming the accuracy of the electromagnetic geophysical probe.

Figure 9a presents averaged electrical conductivity maps, showing measurements ranging from 28.5 mS/m to 42.2 mS/m, Fig. 9b denotes the skin depths corresponding to the frequencies. Three zones, Areas A, B, and C, which are demarcated within the polygon shown in Fig. 9, exhibit diminished conductivity levels. The attenuated conductivity in these areas potentially arises from reduced soil moisture content in compacted strata. Unlike Areas A and C, Area B uniquely exhibits reduced conductivity on its eastern flank, contrasting with the heightened conductivity on the eastern fringes of Areas

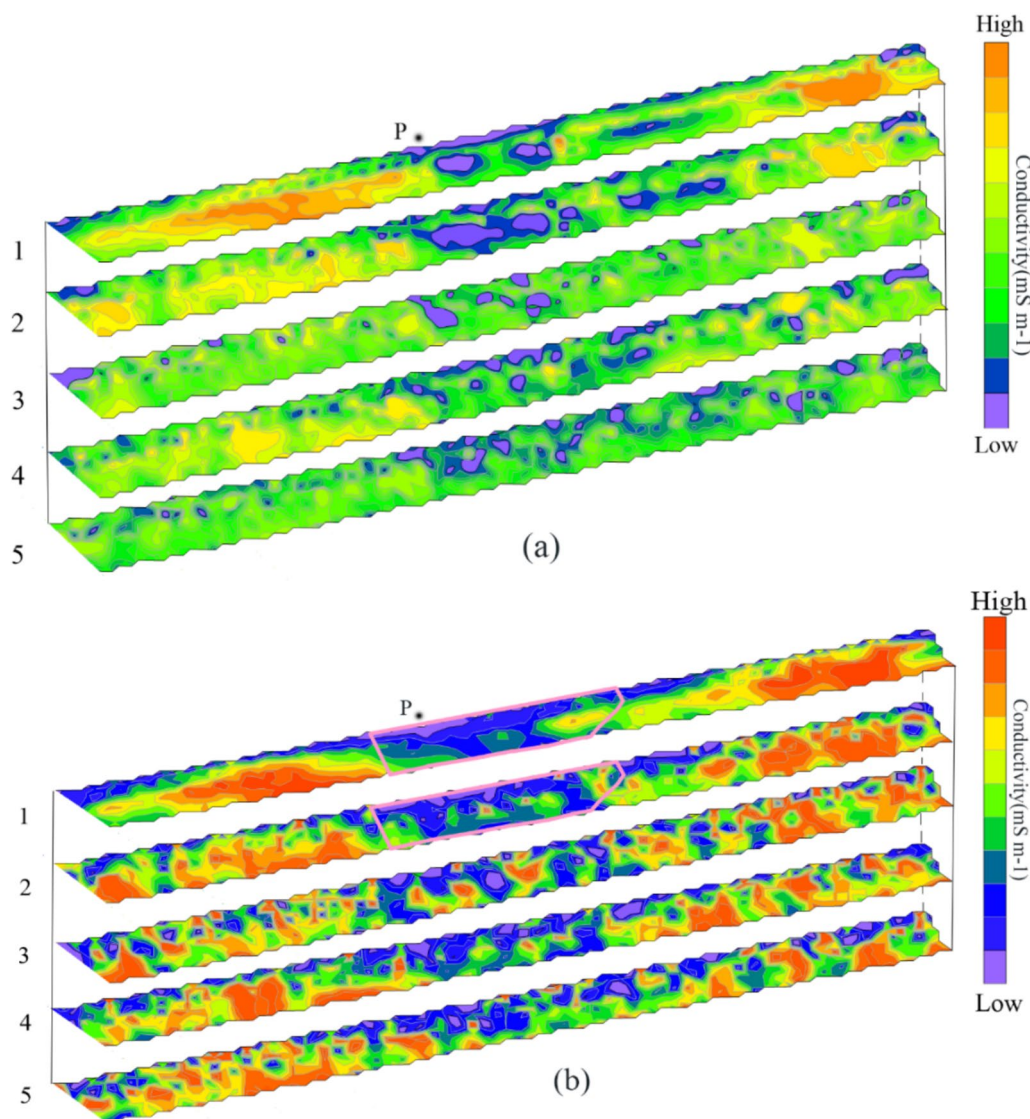


Fig. 8 Represents the conductivity distributions at five different frequencies, from bottom to top: 3025 Hz, 6325 Hz, 13,175 Hz, 27,525 Hz, and 57,525 Hz. **a** is the result of the processing of the collected raw data; **b** is the result of the processing after manual revision, highlighting the occurrence of the tomb passage as marked by pink rectangles

A and C. Local archaeologists have linked this phenomenon to the presence of rammed earth on the west side of the tomb passage detected in Area B. This phenomenon corresponds to the stratification of the soil shown in Fig. 7.

For the No. 1 Mausoleum, Area B has been identified as a tomb passage, and the compaction of the passage with rammed earth occurred during the initial construction phase. To further support this conclusion, we referenced studies on the tomb of Qin Shi Huang, which confirm that rammed earth was an essential component in the original construction of large tombs and associated

structures[66]. Typically, once the mausoleum was constructed, layers of materials such as charcoal, sand, green clay, and rammed earth—or a combination of these—were used to seal the tomb to the surface. This technique was widely applied in the Pre-Qin and Han periods.

Rammed earth was widely utilized in tomb construction, particularly for tomb passages, to ensure structural stability and shield the chambers from environmental stressors. The primary objective was to shield the burial chamber from seasonal variations in temperature and humidity, which could otherwise cause damage to the structure. In most ancient tombs excavated in the Yellow

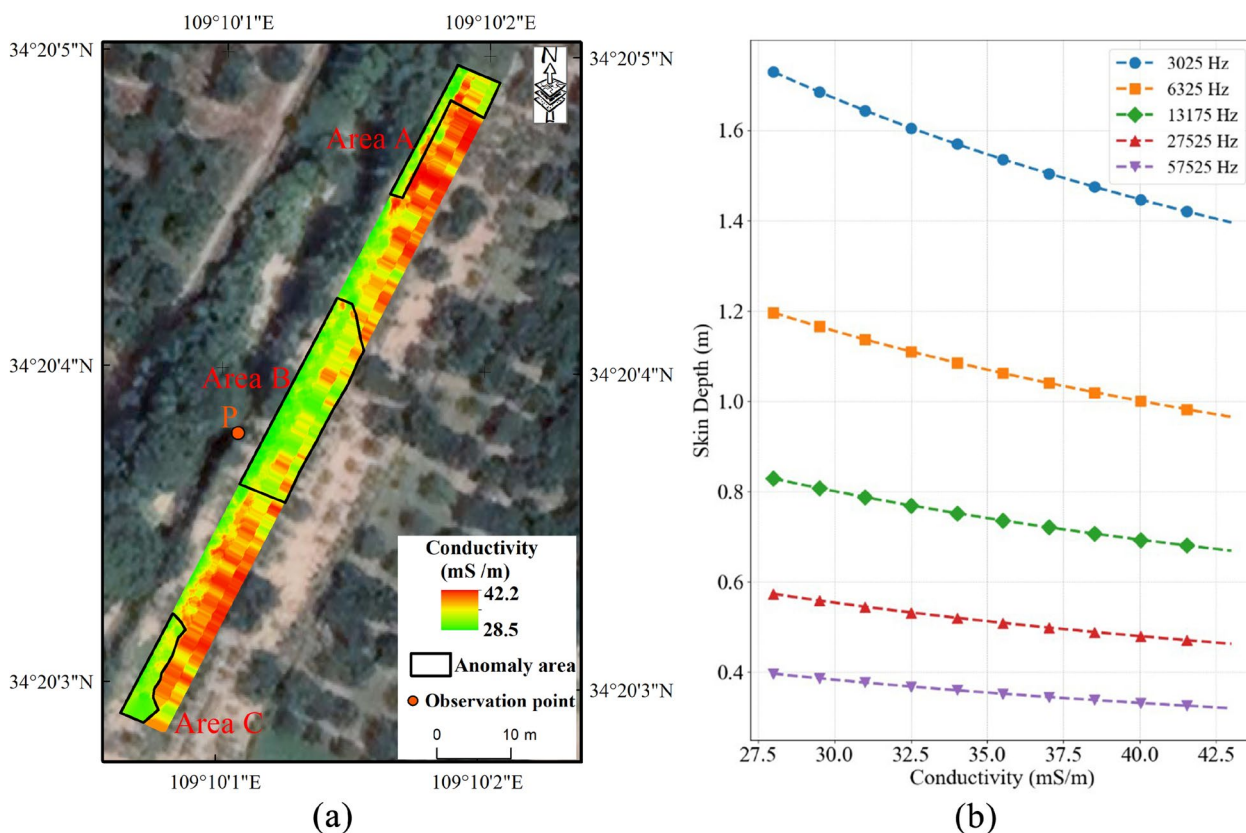


Fig.9 The results of electromagnetic prospecting and the corresponding skin depths at different frequencies are presented. **a** Archaeological evidence confirmed by electromagnetic prospecting is overlaid on the royal tomb, with the average conductivity measurements calculated for five different frequencies, particularly highlighting Area B due to the presence of rammed earth. **b** The skin depth values corresponding to the five frequencies used in the field electromagnetic prospecting

River basin, the tomb walls remain well-preserved, showing minimal signs of damage from rainwater erosion or thawing-induced collapse. This indicates that the tombs underwent specific treatments either during or shortly after excavation, forming part of the standard procedure to ensure long-term preservation.

Remote sensing dynamic monitoring

RS has been proven to be an irreplaceable tool for detecting and monitoring both natural and anthropogenic-induced disturbances for the preventive conservation of heritage sites [67–69]. This study reconstructs the conservation status and evolution of the No. 1 Mausoleum of Qin State over several decades through environmental change detection using Corona imagery from 1970 and GEE imagery from 2018. Figure 10a displays the alteration of the cultural landscape around the No. 1 Mausoleum (marked by green lines). It is evident that village settlements have expanded, accompanied by the construction of connecting roads, as highlighted by the red rectangle. While these facilities improve the living quality

and convenience for local communities, they also pose challenges for site safeguarding due to the enhanced anthropogenic impacts, such as farming and industry.

Besides the boundary gullies, Wangpo Gully in the north and Hanyu Gully in the south, several smaller gullies have developed due to surface changes on the loess ridge where the No. 1 Mausoleum is located. To assess the intensity of these surface changes, smaller gullies were identified using LiDAR-derived DSM data (Fig. 1). Subsequently, we spatially overlaid the 1970 Corona imagery with 2018 GEE imagery on DSM data, enabling detection of changes in gully length from 1970 to 2018.

Figure 10b illustrates the spatial distribution of the developed small gullies on the loess ridge (marked by red lines). Only two sections showed actively developing trends (Table 2), with length increases of 70.3 m (line 5, extending from line 4) and 31.5 m (line 10, extending from line 9), as indicated by the light-blue lines in Fig. 10. These results indicate that surface alterations on the loess ridge have been minimal or negligible over the past decades. Compared to the northwest of the loess plateau in

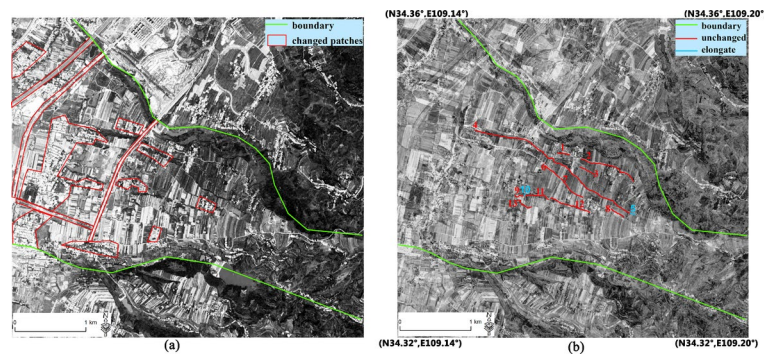


Fig. 10 Comparison results of the 1970 Corona satellite images and the 2018 GEE imagery, including changes in surface cover and gully length. **a** Remote sensing-based change detection to characterize the alteration of the cultural landscape. **b** Quantitative estimation of surface change using the detected changed geometrical indicators, e.g., the length increment of gullies

Table 2 The length of each gully, of which there are both constant and variable-length types

Situation	Number	Length(meters)	
unchanged	4	2616.7	
	8	220.5	
	7	430.5	
	12	610.8	
	11	358.1	
	9	158.8	
	2	186.6	
	13	267.1	
	3	619.2	
	6	271.9	
	1	242.4	
	elongate	5	70.3
		10	31.5

China, the loess particles at this study site (northeastern edge of the Qinling Mountains) are smaller, resulting in a more compacted soil layer that is more resilient to hydrological changes. Additionally, field investigations have revealed that surface changes have not been significant in recent years, as evidenced by the residential houses constructed within these small gullies (Fig. 11); otherwise, the residents' lives and property would be at risk due to potential flooding. This evidence once again confirms the optimized site selection for the Mausoleum, taking into account not only the high and open terrain characteristics but also the skillful utilization of the natural environment to integrate the Mausoleum with the surrounding mountains and water.

Evidence of the Chinese geomancy theory

Chinese Geomancy Theory emphasizes the importance of selecting sites with favorable natural features, particularly the principle of “mountain behind, water in front” which symbolizes protection and prosperity. In this study, we applied a combination of remote sensing data, terrain analysis, and hydrological assessment to evaluate the landscape and validate the application of Feng Shui principles in the site selection of the No.1 Mausoleum of the Eastern Mausoleum of Qin State.

Topography and Elevation: As illustrated in Fig. 12a, the No.1 Mausoleum is located on the piedmont terrace of Lishan Mountain, overlooking Xianyang City to the West-North-West. This positioning aligns with the fundamental Feng Shui concept of having a mountain in the rear, which provides natural protection. To further verify the suitability of this site, we performed terrain analysis using 1 arc-second SRTM DEM data, shown in Fig. 12b. The elevation profile reveals a distinct topographical advantage, with the mausoleum situated on a loess terrace elevated approximately 40 m above the gully floors, significantly exceeding the burial depth of the tomb chambers (less than 30 m). This elevated positioning not only offers protection from potential flooding but also aligns with the Feng Shui requirement of an elevated, protected site, ensuring both security and symbolic strength.

Water Features and Drainage: The proximity to four major river channels, as shown in Fig. 12a, further supports the principle of “water in front.” The Wei River, flowing through Xianyang City and merging with the Jing River, along with the Ba and Chan Rivers, traverses the western foothills of Lishan Mountain. This hydrological arrangement meets the Feng Shui criterion of a site with beneficial water flow, symbolizing prosperity. Additionally, hydrological analysis of the DEM data confirmed that the nearby gullies serve as effective drainage

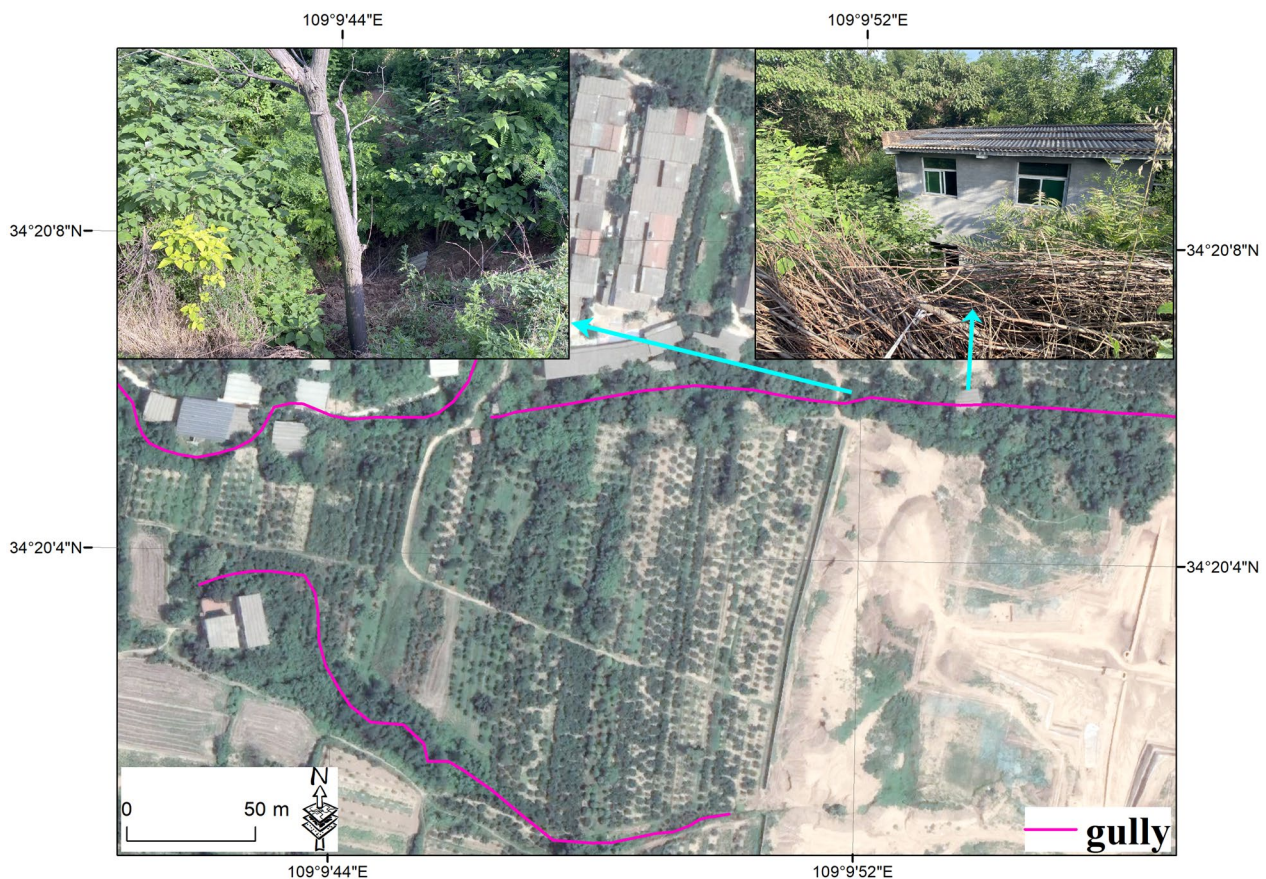


Fig. 11 Residential houses built on the gully observed from the field campaign in 2023, and the gullies has been eroded over the years but is not deep, only about 0.5m deep

channels, minimizing the risk of water accumulation at the tomb site. The strategic positioning of the mausoleum on elevated ground, combined with the natural drainage provided by the gullies, ensures protection against water damage, which is critical in Feng Shui considerations for site preservation and environmental harmony.

Discussion and conclusion

Space archaeological prospecting and dynamic monitoring are crucial for exploiting the archaeological value and ensuring the sustainable development of the Mausoleum. These efforts address gaps in research and deepen understanding of the site. This study employed multi-modal space-ground observations and derivative RS products to test the viability of non-invasive RS technologies in archaeology and site conservation. The site was delineated using Corona imagery, yielding clear demarcations between the Mausoleum and its surroundings. Furthermore, multi-temporal Sentinel-2 data were used to compute temporally averaged NDVI and NDMI indices, highlighting emerging vegetation and soil archaeological marks. Disturbances from ancient artifacts resulted in

suppressed NDVI values and traces of hydrological signatures (NDMI values), particularly near the No.1 Mausoleum. Additionally, thermal anomalies were detected using surface temperature data from SDGSAT-1 thermal infrared images, emphasizing the importance of observation season and timing in identifying thermal archaeological signs. GEM-2 electromagnetic prospecting and field investigations confirmed the effectiveness of RS in archaeology, including the discovery of ancient tomb passages corroborated by local archaeologists. Chinese Geomancy Theory, which influenced mausoleum site selection in ancient times, was evaluated through terrain-based landscape analysis and hydrological investigation. The results demonstrate that the royal tombs benefit from splendid views and disturbance avoidance. The No.1 Mausoleum, situated on the loess ridge at the western piedmont of Lishan Mountain, forms a natural barrier that enhances the secrecy and defensiveness of the site; its proximity to Xianyang, the Qin State dynasty's capital, facilitates ceremonies and other activities. The surrounding complex topography, with undulating hills and deep gullies, provides a natural defense against land

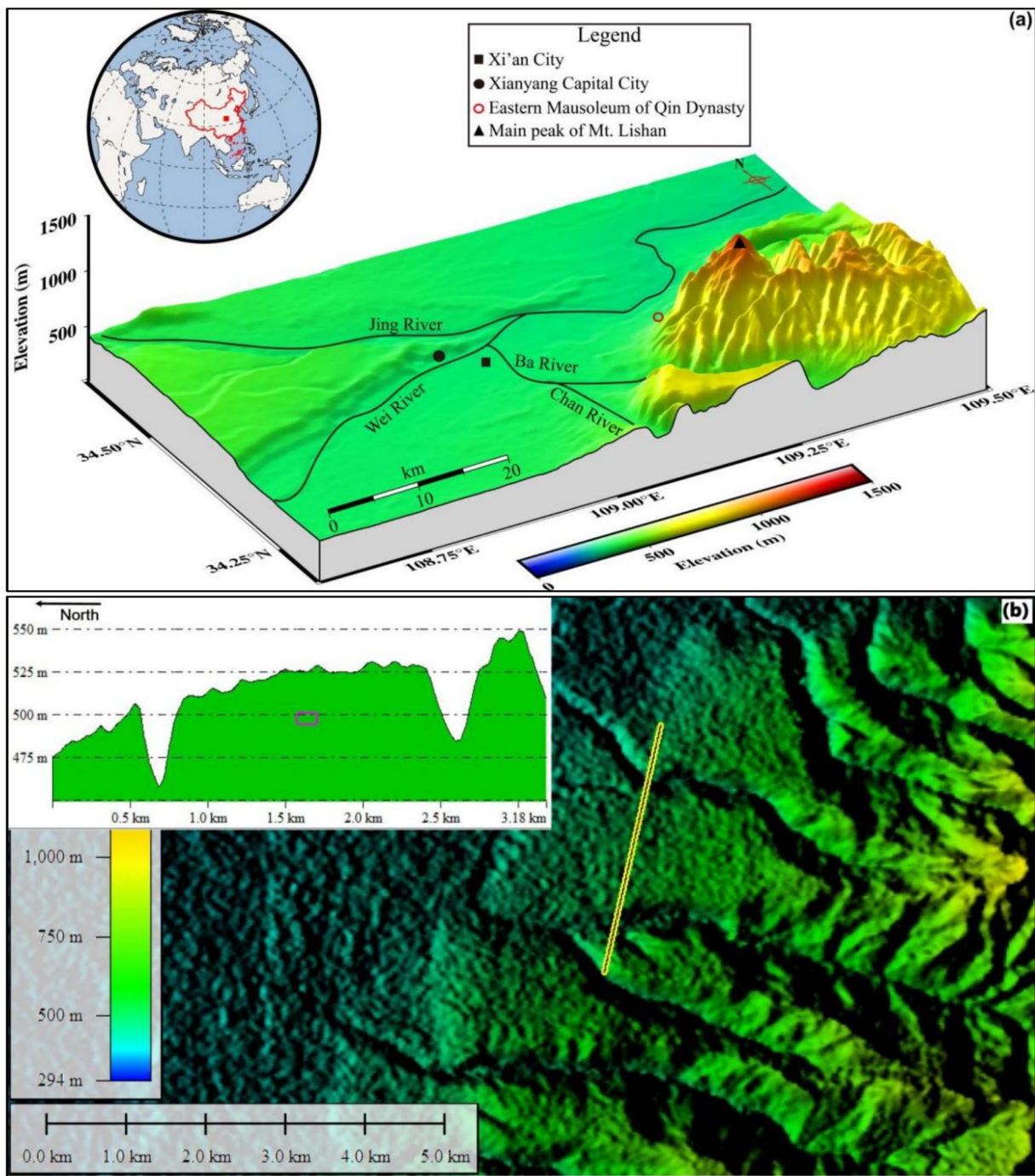


Fig.12 Optimized site selection for the royal tombs. **a** Landscape and **b** disaster avoidance perspectives (the coffin chamber is marked by the yellow rectangle)

use encroachment and potential natural disasters such as flooding. Surface changes around the mausoleum on the loess ridge have been too mild to affect the preservation conditions, a fact confirmed by the physical characteristics of loess (small particles and compact soil layers) and by observing landcover changes from Corona and GEE imagery over approximately five decades. This evidence supports the optimal site selection for the mausoleum, adhering to Chinese Geomancy Theory, particularly the principle of harmony between humanity and nature.

Acknowledgements

We acknowledge the joint funding from the National Natural Science Foundation of China (NSFC) [Grant No. 42271327] and the Innovative Research Program of the International Research Center of Big Data for Sustainable Development Goals [Grant No. CBAS2022IRP06].

Author contributions

Designed research: F Chen. Performed research: Y Luo and F Chen. Analyzed data: Y Luo, F Chen, S Gao, M Zhu, W Zhou. Wrote the paper: Y Luo, F Chen, and A Elfadaly.

Data availability

The authors confirm that the data supporting the findings of this study are available within the article.

Declarations

Competing interests

The authors declare that they have no known competing financial interests or personal relationships that could have appeared to influence the work reported in this paper.

Received: 6 June 2024 Accepted: 5 October 2024
Published online: 14 October 2024

References

- Reimann L, Vafeidis AT, Brown S, Hinkel J, Tol RSJ. Mediterranean UNESCO world heritage at risk from coastal flooding and erosion due to sea-level rise. *Nat Commun*. 2018;9(1):4161. <https://doi.org/10.1038/s41467-018-06645-9>.
- Sesana E, Gagnon AS, Ciantelli C, Cassar J, Hughes JJ. Climate change impacts on cultural heritage: A literature review. *Wiley Interdiscip Rev-Clim Change*. 2021. <https://doi.org/10.1002/wcc.710>.
- Masini N, Lasaponara R. Satellite-based recognition of landscape archaeological features related to ancient human transformation. *J Geophys Eng*. 2006;3(3):230–5. <https://doi.org/10.1088/1742-2132/3/3/004>.
- Xiao D, Lu L, Wang X, Nitivattananon V, Guo H, Hui W. An urbanization monitoring dataset for world cultural heritage in the Belt and Road region. *Big Earth Data*. 2022;6(1):127–40. <https://doi.org/10.1080/20964471.2020.1853362>.
- Tie YY. On Liao dynasty tombs and geomancy. Changchun: Bachelor, Changchun Normal University; 2012.
- Gao F. Funeral Feng Shui and Burial Sites in the Qin and Han Dynasties. *Qin and Han studies*. 2013;00:223–30.
- Yan QY. Cliff Burials and Feng Shui Beliefs—an examination centered on Guizhou Region. *J Central South Univ Natl*. 2016;36(02):56–60.
- Feng C. The Politics of Feng Shui: Society, market and state in the spatial order of burial in rural China. *J Shanxi Agric Univ*. 2022;21(04):74–84. <https://doi.org/10.13842/j.cnki.issn1671-816x.2022.04.008>.
- Tan K, Wan Y, Zhou X, Song D, Duan Q. The application of remote sensing technology in the archaeological study of the Mausoleum of Emperor Qinshihuang. *Int J Remote Sens*. 2006;27(16):3347–63. <https://doi.org/10.1080/01431160600554389>.
- Blänsdorf C, Yin X. A colourful world for the Emperor's Soul: the polychromy of the terracotta sculptures at Qin Shihuang's burial complex. *Stud Conserv*. 2006;51(sup2):177–83. <https://doi.org/10.1179/sic.2006.51.Supplement-2.177>.
- Huan Y, Jizhen L, Eckfeld T, Junchang Y. Making the first emperor's chariots—high-temperature bronze connection technologies in Qin dynasty China. *AICCM Bulletin*. 2021;42(2):91–103. <https://doi.org/10.1080/10344233.2022.2131197>.
- Wynn JC, Lasca NP, Donahue J. Applications of high-resolution geophysical methods to archaeology. *Geol Soc Am*. 1990. <https://doi.org/10.1130/DNAG-CENT-v4.603>.
- Theocaris PS, Liritzis I, Lagios E, Sampson A. Geophysical prospection, archaeological excavation, and dating in two Hellenic pyramids. *Surv Geophys*. 1996;17(5):593–618. <https://doi.org/10.1007/BF01888980>.
- Gaffney C, Gaffney V. Non-invasive investigations at Wroxeter at the end of the twentieth century. *Archaeol Prospect*. 2000;7(2):65–7.
- Lucas R, Rowlands, Niemann K, Merton R. Hyperspectral sensors: past, present and future. 2004: 11–49.
- Rowlands A, Sarris A. Detection of exposed and subsurface archaeological remains using multi-sensor remote sensing. *J Archaeol Sci*. 2007;34(5):795–803.
- Ireland T. Up close and personal: feeling the past at urban archaeological sites. *Public His Rev*. 2016. <https://doi.org/10.5130/phrj.v23i0.5332>.
- Argyrou A, Agapiou A. A review of artificial intelligence and remote sensing for archaeological research. *Remote Sensing*. 2022. <https://doi.org/10.3390/rs14236000>.
- Wondie M, Schneider W, Melesse AM, Teketay D. Spatial and temporal land cover changes in the Simen Mountains National Park, a world heritage site in Northwestern Ethiopia. *Remote Sensing*. 2011;3(4):752–66. <https://doi.org/10.3390/rs3040752>.
- Tapete D, Cigna F. Trends and perspectives of space-borne SAR remote sensing for archaeological landscape and cultural heritage applications. *J Archaeol Sci-Rep*. 2017. <https://doi.org/10.1016/j.jasrep.2016.07.017>.
- Bai XY, Du PJ, Guo SC, Zhang P, Lin C, Tang PF, Zhang C. Monitoring land cover change and disturbance of the Mount Wutai world cultural landscape heritage protected area, based on remote sensing time-series images from 1987 to 2018. *Remote Sensing*. 2019. <https://doi.org/10.3390/rs11111332>.
- Chen FL, Zhou W, Tang YW, Li R, Lin H, Balz T, et al. Remote sensing-based deformation monitoring of pagodas at the Bagan cultural heritage site, Myanmar. *Int J Dig Earth*. 2022;15(1):770–88. <https://doi.org/10.1080/17538947.2022.2062466>.
- Chen F, Masini N, Liu J, You J, Lasaponara R. Multi-frequency satellite radar imaging of cultural heritage: the case studies of the Yumen Frontier Pass and Niya ruins in the Western Regions of the Silk road Corridor. *Int J Digital Earth*. 2016;9(12):1224–41. <https://doi.org/10.1080/17538947.2016.1181213>.
- Chen F, Jiang A, Tang P, Yang R, Zhou W, Wang H, Lu X, Balz T. Multi-scale synthetic aperture radar remote sensing for archaeological prospection in Han Hangu Pass, Xin'an China. *Remote Sensing Lett*. 2017;8(1):38–47. <https://doi.org/10.1080/2150704X.2016.1235812>.
- Cigna F, Balz T, Tapete D, Caspari G, Fu B, Abballe M, Jiang H. Exploiting satellite SAR for archaeological prospection and heritage site protection. *Geo-spatial Inf Sci*. 2023. <https://doi.org/10.1080/10095020.2023.2223603>.
- Parcak S. Satellite remote sensing methods for monitoring archaeological tells in the middle east. *J Field Archaeol*. 2007;32(1):65–81. <https://doi.org/10.1179/009346907791071773>.
- Jiang AH, Chen FL, Tang PP, Liu GL, Liu WK, Wang HC, Lu X, Zhao XL. Radar remote sensing for archaeology in Hangu Frontier Pass in Xin'an, China. In: *IOP Conference Series: Earth and Environmental Science*, IOP Publishing: China. 2017; 57: pp.012031. <https://doi.org/10.1088/1755-1315/57/1/012031>.
- Li ZL, Tang BH, Wu H, Ren HZ, Yan GJ, Wan ZM, Trigo IF, Sobrino JA. Satellite-derived land surface temperature: current status and perspectives. *Remote Sensing Environ*. 2013. <https://doi.org/10.1016/j.rse.2012.12.008>.
- Guo H, Dou C, Chen H, Liu J, Fu B, Li X, Zou Z, Liang D. SDGSAT-1: the world's first scientific satellite for sustainable development goals. *Sci Bull*. 2023;68(1):34–8. <https://doi.org/10.1016/j.scib.2022.12.014>.

30. Leckebusch J. Ground-penetrating radar: a modern three-dimensional prospection method. *Archaeol Prospect*. 2003. <https://doi.org/10.1002/arp.211>.
31. Huang H, Won IJ. Real-time resistivity sounding using a hand-held broad-band electromagnetic sensor. *Geophysics*. 2003;68(4):1224–31. <https://doi.org/10.1190/1.1598114>.
32. He X, Wang H, Ma S. Translation algorithm of the apparent conductivity using the frequency-domain electromagnetic method of a magnetic dipole. *J Appl Geophys*. 2017. <https://doi.org/10.1016/j.jappgeo.2017.09.015>.
33. Huang C, Chen Y, Zhang S, Wu J. Detecting, extracting, and monitoring surface water from space using optical sensors: a review. *Rev Geophys*. 2018;56(2):333–60. <https://doi.org/10.1029/2018rg000598>.
34. Li M. Dynamic monitoring algorithm of natural resources in scenic spots based on MODIS Remote Sensing technology. *Earth Sci Res J*. 2021;25(1):57–64. <https://doi.org/10.15446/esrj.v25n1.93869>.
35. Xu J, Esamdin A, Feng G-J, Pu G-X, Hu Y, Hu K-L, et al. Site-testing at Muztagh-ata site III: temperature inversion in surface-layer atmosphere. *Res Astron Astrophys*. 2020. <https://doi.org/10.1088/1674-4527/20/6/88>.
36. Jiao NF, Li G. A preliminary study of the problems associated with the “East Mausoleum of Qin.” *Archaeol Antiquities*. 2021;01:94–9.
37. Altaweel M. The use of ASTER satellite imagery in archaeological contexts. *Archaeol Prospect*. 2005; <https://doi.org/10.1002/arp.254>.
38. Sarris A, Papadopoulos N, Agapiou A, Salvi MC, Hadjimitsis DG, Parkinson WA, Yerkes RW, Gyucha A, Duffy PR. Integration of geophysical surveys, ground hyperspectral measurements, aerial and satellite imagery for archaeological prospection of prehistoric sites: the case study of Vésztő-Mágor tell, Hungary. *J Archaeol Sci*. 2013;40(3):1454–70. <https://doi.org/10.1016/j.jas.2012.11.001>.
39. Masini N, Lasaponara R. Investigating the spectral capability of QuickBird data to detect archaeological remains buried under vegetated and not vegetated areas. *J Cult Herit*. 2007;8(1):53–60. <https://doi.org/10.1016/j.culher.2006.06.006>.
40. Saturno W, Sever TL, Irwin DE, Howell BF, Garrison TG. Putting us on the map: Remote sensing investigation of the ancient Maya landscape WISE-MAN J, EL-BAZ F. *Remote Sensing in Archaeology*. New York, NY; Springer New York. 2007: 137–60. https://doi.org/10.1007/0-387-44455-6_6.
41. Garrison TG, Houston SD, Golden C, Inomata T, Nelson Z, Munson J. Evaluating the use of IKONOS satellite imagery in lowland Maya settlement archaeology. *J Archaeol Sci*. 2008;35(10):2770–7. <https://doi.org/10.1016/j.jas.2008.05.003>.
42. Pappu S, Akhilesh K, Ravindranath S, Raj U. Applications of satellite remote sensing for research and heritage management in Indian prehistory. *J Archaeol Sci*. 2010;37(9):2316–31. <https://doi.org/10.1016/j.jas.2010.04.005>.
43. Lasaponara R, Masini N. On the potential of QuickBird data for archaeological prospection. *International Journal of Remote Sensing—INT J REMOTE SENS*. 2006. <https://doi.org/10.1080/01431160500333983>.
44. Lasaponara R, Lanorte A, Coluzzi R, Masini N. Performance evaluation of data fusion techniques for archaeological prospection based on satellite data. In: *Remote Sensing for Environmental Monitoring, GIS Applications, and Geology VII: Proceedings of SPIE—The International Society for Optical Engineering*, SPIE: Italy. 2007. <https://doi.org/10.1117/12.738204>.
45. Rokni K, Ahmad A, Selamat A, Hazini S. Water feature extraction and change detection using multitemporal Landsat imagery. *Remote Sensing*. 2014;6(5):4173–89. <https://doi.org/10.3390/rs6054173>.
46. Duan T, Chapman SC, Guo Y, Zheng B. Dynamic monitoring of NDVI in wheat agronomy and breeding trials using an unmanned aerial vehicle. *Field Crops Res*. 2017. <https://doi.org/10.1016/j.fcr.2017.05.025>.
47. Hassan MA, Yang M, Rasheed A, Yang G, Reynolds M, Xia X, Xiao Y, He Z. A rapid monitoring of NDVI across the wheat growth cycle for grain yield prediction using a multi-spectral UAV platform. *Plant Sci*. 2019. <https://doi.org/10.1016/j.plantsci.2018.10.022>.
48. Poussin C, Massot A, Ginzler C, Weber D, Chatenoux B, Lacroix P, Pillier T, Nguyen L, Giuliani G. Drying conditions in Switzerland—indication from a 35-year Landsat time-series analysis of vegetation water content estimates to support SDGs. *Big Earth Data*. 2021;5(4):445–75. <https://doi.org/10.1080/20964471.2021.1974681>.
49. Qin Z, Karnieli A, Berliner P. A mono-window algorithm for retrieving land surface temperature from Landsat TM data and its application to the Israel-Egypt border region. *Int J Remote Sens*. 2001;22(18):3719–46. <https://doi.org/10.1080/01431160010006971>.
50. Jimenez-Munoz JC, Sobrino JA, Skokovic D, Mattar C, Cristobal J. Land surface temperature retrieval methods from Landsat-8 thermal infrared sensor data. *IEEE Geosci Remote Sensing Lett*. 2014;11(10):1840–3. <https://doi.org/10.1109/lgrs.2014.2312032>.
51. Shahraki H, Moradi S, Aalaei S. Infrared target detection based on the single-window average absolute gray difference algorithm. *SIVIP*. 2021;16(3):857–63. <https://doi.org/10.1007/s11760-021-02027-9>.
52. Huang MF, Bo C, Can C, Su-Hong L, Rui P. The urban temperature abnormal analysis based on the Landsat5/TM data. In: Huang MF, Bo C, Can C, Su-Hong L, Rui P, editors. 2006 IEEE international symposium on geoscience and remote sensing. USA: IEEE; 2006. <https://doi.org/10.1109/IGARSS.2006.877>.
53. Qin ZH, Li WJ, Zhang MH, Berli AKP. The estimation of land surface emissivity for Landsat TM6. *Remote Sensing for Land Res*. 2011;16:28.
54. SDGs. Handbook of SDGSAT-1 Satellite Products (Version 1.0). 2022. <http://124.16.184.48:6008/download>. Accessed 22 Jul 2023.
55. Sobrino JA, Raissouni N, Li ZL. A comparative study of land surface emissivity retrieval from NOAA data. *Remote Sens Environ*. 2001;75(2):256–66. [https://doi.org/10.1016/s0034-4257\(00\)00171-1](https://doi.org/10.1016/s0034-4257(00)00171-1).
56. Stathopoulou M, Cartalis C, Petrakis M. Integrating corine land cover data and Landsat TM for surface emissivity definition: application to the urban area of Athens, Greece. *Int J Remote Sensing*. 2007;28(15):3291–304. <https://doi.org/10.1080/01431160600993421>.
57. Sekertekin A, Bonafoni S. Land surface temperature retrieval from Landsat 5, 7, and 8 over rural areas: assessment of different retrieval algorithms and emissivity models and toolbox implementation. *Remote Sensing*. 2020. <https://doi.org/10.3390/rs12020294>.
58. Guo JM, Shi JY, Han XY, Zheng TF, Wang Q. Inversion land surface temperature by using TM data. In: Guo JM, editor. *Remote sensing and modeling of ecosystems for sustainability IX*. California: SPI; 2012. <https://doi.org/10.1117/12.930428>.
59. Kaufman YJ, Gao BC. Remote sensing of water vapor in the near IR from EOS/MODIS. *IEEE Trans Geosci Remote Sens*. 1992;30(5):871–84. <https://doi.org/10.1109/36.175321>.
60. Hu DY, Qiao K, Wang XL, Zhao LM, Ji GH. Land surface temperature retrieval from Landsat 8 thermal infrared data using mono-window algorithm. *J Remote Sensing*. 2015;19(06):964–76. <https://doi.org/10.11834/jrs.20155038>.
61. Ding LD, Qin ZH, Mao KB. A research of split window algorithm based on MODIS image data and parameter determination. *Remote Sensing Technol Appl*. 2005;02:284–9. <https://doi.org/10.3969/j.issn.1004-0323.2005.02.014>.
62. Won IJ. A wide-band electromagnetic exploration method—some theoretical and experimental results. *Geophysics*. 1980;45(5):928–40.
63. Yu L, Zhang Y, Nie Y, Zhang W, Gao H, Bai X, Liu Y, Hategekimana Y, Zhu J. Improved detection of archaeological features using multi-source data in geographically diverse capital city sites. *J Cult Herit*. 2018. <https://doi.org/10.1016/j.culher.2018.01.001>.
64. Song T, Duan Z, Liu JZ, Shi JZ, Yan F, Sheng SJ, Jun H, Wu W. Comparison of surface temperature inversion algorithms for Landsat 8 data. *J Remote Sensing*. 2015;19(03):451–64. <https://doi.org/10.11834/jrs.20154180>.
65. He X. Research on GEM-2 data processing and inversion methods and their application to sea ice thickness detection. Hangzhou: Master, Zhejiang University; 2018.
66. Duan Q. A study of issues related to the mausoleum of the first Qin emperor. Seattle: Doctor Northwest University; 2007.
67. D’orazio T, Da Pelo P, Marani R, Guaragnella C. Automated extraction of archaeological traces by a modified variance analysis. *Remote Sensing*. 2015;7(4):3565–87. <https://doi.org/10.3390/rs70403565>.
68. Ye P. Remote sensing approaches for meteorological disaster monitoring: Recent achievements and new challenges. *Int J Environ Res Public Health*. 2022. <https://doi.org/10.3390/ijerph19063701>.
69. Wu G, Dang A, Chen M, Li X. Study on historical cities conservation monitoring supported by high-resolution remote sensing. *Int Rev Spat Planning Sustain Dev*. 2023;11(2):258. https://doi.org/10.14246/irpsd.11.2_240.

Publisher's Note

Springer Nature remains neutral with regard to jurisdictional claims in published maps and institutional affiliations.